Self-Assembled On-Chip-Integrated Giant Magneto-Impedance Sensorics

Daniil Karnaushenko, Dmitriy D. Karnaushenko, Denys Makarov,* Stefan Baunack, Rudolf Schäfer, and Oliver G. Schmidt*

Encephalography techniques, especially those based on the detection of electrical potential, are commonly applied in medical institutions worldwide for health monitoring, e.g., diagnosis of epilepsy,[1] tremor,[2] or depressions[3] and are now entering the new field of interfacing the human brain with smart prosthetics.[4,5] Its magnetic counterpart, namely magnetoencephalography, relies on the detection of tiny magnetic fields generated by the electrical currents in the nervous system.[6,7] Being able to provide the same physiological information as the conventional electroencephalography,[8] magnetoencephalography offers strong advantages in terms of sensitivity and the opportunity to identify diseases, e.g., epilepsy at early stages with great spatial localization.[9] A standard magnetoencephalography equipment is based on superconducting quantum interference devices (SQUIDs)[6] or hybrid systems combining superconducting flux transformers with magneto-resistive sensorics.[10] Although SQUID-based devices have proven their relevance in neurological disease treatment,[11] rather high fabrication and maintenance costs limit their wide spread applicability. Furthermore, as SQUIDs need permanent cooling with liquid helium, the resulting setup has high maintenance cost, and is bulky and heavy, thus limiting the mobility of the patients. The development of a cost-efficient yet high-performance and even portable magnetoencephalography equipment would bring these unique devices to regular medical institutions, offering early stage disease diagnostics with great spatial resolution hence helping to minimize invasivity upon surgical treatment. Furthermore, if achieved, portable as well as light-weight magnetoencephalography devices bear a great potential to revolutionize the field of smart prosthetics,[4] brain–machine and brain–brain interfaces due to a precise volumetric localization and characterization of current elements that correspond to particular mental activity and that are not accessible directly by electroencephalography and electrocorticography techniques.[12]

The realization of this ambitious goal requires new sensor solutions offering cost-efficient room temperature access to the tiny magnetic fields stemming from the brain activity in the neural tissue.[13] In this respect, atom vapor magnetometers[13,14] were recently suggested as an alternative to SQUIDs for magnetoencephalography applications. However, the need of vacuum packaging of the measurement cell and optical pumping makes these devices rather complex in fabrication and in operation. Hence, there is a need to develop simple use, cost-efficient, and all-electrical measurement schemes for magnetoencephalography equipment, which would be in the spirit of the conventional electroencephalography devices.

To this end, magnetic field sensorics has benefited from the discovery of the new effect in magnetically coated nonmagnetic microwires known as the giant magneto-impedance (GMI).[15–18] The GMI effect resembles itself as large variation of real and imaginary parts of the complex impedance of the sensor, driven with an alternating current (AC), when exposed to a magnetic field. The GMI devices operate at room temperatures[17,19] and reveal remarkable sensitivity to small magnetic fields down to pico-Tesla regime.[18,20–24] Although the GMI effect does not have a long history, it is already implemented in devices applied in automotive, space, and medical sectors.[23,25]

Cost efficiency and high universality suggest extensive applications of GMI devices in biology and medicine for, e.g., noninvasive monitoring of biomagnetic fields.[26,27] However, the microwire GMI sensor elements cannot be produced in a CMOS compatible way due to the stringent requirements on the fabrication involving rapid quenching of molten magnetic alloys to achieve circumferential magnetization[25] and the need to be combined with pick-up coils[17] to enhance the sensitivity. Therefore, the state-of-the-art GMI sensorics resemble itself as

D. Karnaushenko, D. D. Karnaushenko, Dr. D. Makarov, Dr. S. Baunack, Prof. O. G. Schmidt
Institute for Integrative Nanosciences
Leibniz Institute for Solid State and Materials Research Dresden (IFW Dresden)
01069 Dresden, Germany
E-mail: d.karnaushenko@ifw-dresden.de; d.makarov@ifw-dresden.de

Prof. R. Schäfer
Institute for Metallic Materials
Leibniz Institute for Solid State and Materials Research Dresden (IFW Dresden)
01069 Dresden, Germany

Prof. R. Schäfer
Institute for Materials Science
Dresden University of Technology
01069 Dresden, Germany

Prof. O. G. Schmidt
Material Systems for Nanoelectronics
Chemnitz University of Technology
09107 Chemnitz, Germany

Prof. O. G. Schmidt
Center for Advancing Electronics Dresden
Dresden University of Technology
01062 Dresden, Germany

DOI: 10.1002/adma.201503127

hybrid microelectronic devices with the need to bond the GMI wire to the CMOS-based conditioning electronics, thus limiting the total number of sensing elements.[28] This is a clear disadvantage for magnetoencephalography applications where a spatial mapping of the magnetic field requires sensor arrays of at least 200 GMI devices to be compatible with the current SQUID-based technology. Thin film fabrication technologies emerged as an integrated circuit friendly alternative to the wire-based technology, potentially allowing the fabrication of sensor arrays.[29,30] However, due to the planar configuration of magnetic layers, it is still required to define a transversal to the wire axis magnetization by annealing the planar structures at temperatures beyond 200 °C at applied electric currents of at least 30 mA. This process is difficult to realize on an integrated circuit for a single sensor and even more difficult for array configurations.[31,32] Hence, a viable technology platform should be developed to produce arrays of compact GMI sensing elements with defined circumferential anisotropy in a CMOS compatible way.

Here, we apply strain engineering[33–36] to realize arrays of GMI sensors, which are directly on-chip integratable in a CMOS compatible process. We put forth a new platform[37] that is relying on photopatternable, thermally and chemically stable imide- and acrylic-based polymers allowing for the stimuli-controlled self-assembly of initially planar NiFe-/Cu/NiFe-based heterostructures into 3D tubular architectures possessing the GMI functionality. In this way, we overcome the most crucial aspect in GMI fabrication technology, i.e., the formation of a circular magnetization, thus avoiding high temperature processing with applied electric current and allowing for the direct fabrication of sensor arrays on the integrated circuit. The NiFe/Cu/NiFe stacks are chosen as model prototype GMI systems revealing a stable effect with an amplitude in the range of 50%/Oe below 100 MHz excitation frequency and characteristics suitable for lab investigations.[38,39]

The developed technology platform supports the integration of multiple functional elements, including pick-up coils and GMI sensors, into a single tubular architecture with a typical length of 2 mm and a diameter of some tens of micrometer. A characterization of the GMI sensing elements before and after the self-assembly process reveals that their magneto-electrical performance is drastically improved up to 80 times when transformed into a 3D architecture. This improvement is due to a geometrically induced circumferential magnetization achieved upon transforming the initial planar sensor into the tubular architecture. Furthermore, the integrated pick-up coil allows for a bipolar response of the devices. These compact GMI sensors equipped with pick-up coils operate at ambient condition and demonstrate rather strong responsiveness to small magnetic fields of 45 μV Oe^{-1} at a remarkably small excitation current of 1 mA. Independent of its compactness, the performance of the rolled-up GMI sensors is in the range of the state-of-the-art GMI devices. We note that the low excitation current of 1 mA and frequencies below 100 MHz are chosen to comply with the safety regulations accordingly to the "IEEE Standard for Safety Levels with Respect to Human Exposure to Radio Frequency Electromagnetic Fields, 3 kHz to 300 GHz."[40] With these parameters, the maximum AC magnetic field produced by the GMI element with a typical length below 10 mm is in the range of 10 nT, i.e., well within the safety limits of 100 nT.

The realization of complex electronic components, e.g., sensors with pick-up coils, requires multiple fabrication steps including deposition and lithography to be carried out. Microelectronics processing as typically used in CMOS technology relies on photopatterning of polymers offering immediate batch fabrication while processing the structures on planar 2D substrates like silicon and glass. To allow for the self-assembly of the initially planar devices into compact 3D tubular structures, we propose to use stimuli-responsive polymers,[41,42] which develop a differential strain during water uptake relying on reinforcement layers.[35,43] Similar complex polymeric heterostructures were already successfully applied to fabricate self-assembled 3D objects including pyramids,[35] stars,[44] cubes,[45] as well as tubular architectures.[46,47] Despite a broad variety of technological solutions, the state-of-the-art polymeric platforms applied for strain engineering[44,48–50] are typically relying on a single-step lithography. Hence, they do not allow the fabrication of microelectronic devices owing to a chemical incompatibility among the fabrication steps, especially the use of various polar and nonpolar solvents including strong base and acidic solutions during lithographic processing. In this respect, the largest concern is about the stability of the functional polymeric layer stack (sacrificial, stimuli-responsive layer, and reinforcing layers). The sacrificial layer should withstand all the processing steps without degrading its ability to be selectively dissolved after all the processing is finished. Furthermore, the stimuli-responsive layer must not be activated during all the processing steps of the devices. In turn, it should be assured that the self-assembly process, which include etching of the sacrificial layer and swelling of the stimuli-responsive layer does not disturb the magnetic, electrical as well as the mechanical properties of the functional layer stack to assure a high fabrication yield. These strict requirements impose strict limitations on the choice of the sacrificial layer as well as strained bilayer.

To overcome these limitations, we put forth an alternative strain engineering technology platform relying on photopatternable, thermally, and chemically stable imide- and acrylic-based polymers. To this end, we formulated and synthesized a metal-organic sacrificial layer, a novel stimuli-responsive hydrogel, stiff polyimides as reinforcement layers, and a polychloroprene-based passivation polymer. These layers are stable at high temperatures up to 270 °C and inert in common organic nonpolar, polar protic, and aprotic solvents, as well as in moderate bases and acids allowing for multiple lithography steps. The stack of the three polymers, namely the sacrificial layer (thickness: 160 nm), hydrogel-based swelling layer (thickness: 180 nm), and stiff polyimide-based reinforcement layer (thickness: 700 nm), is prepared onto a 22×22 mm^2 glass substrate. Using optical lithography, we define sites for the GMI sensors by patterning the functional stack to achieve arrays of squares or rectangles with a typical size in the range of 1×1 mm^2 (**Figure 1**a1). Our technology allows to process up to 400 devices over the entire 22×22 mm^2 substrate in a single fabrication run. Onto these predetermined areas, we prepare a lift-off photoresist mask to define in a single-step electrical contacts and a pick-up coil with a conductor width of 40 μm by depositing Cr(5 nm)/Au(50 nm) bilayers using electron beam

ADVANCED MATERIALS
www.advmat.de

www.MaterialsViews.com

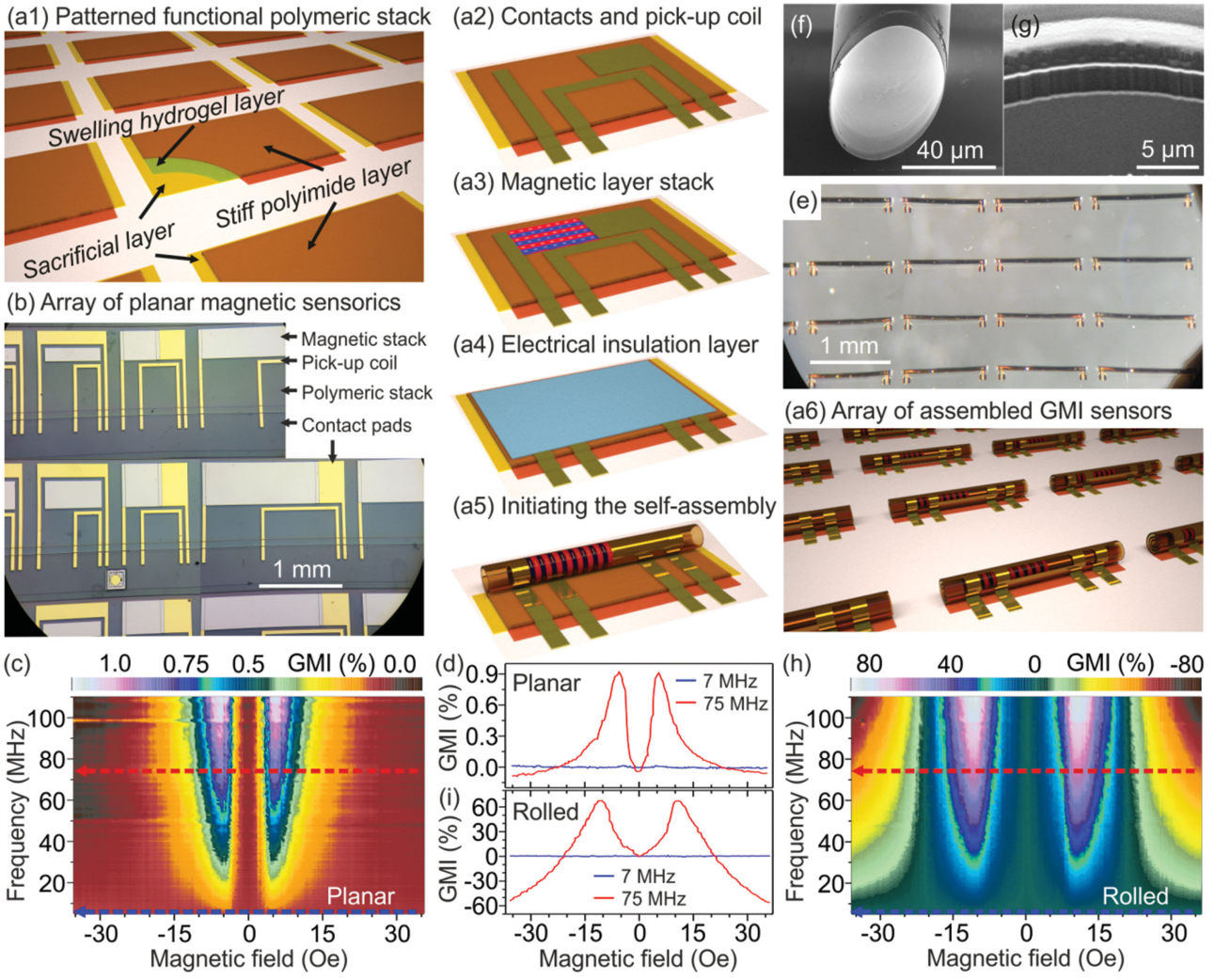

Figure 1. Fabrication and characterization of on-chip-integrated GMI sensorics: a) Schematics illustrating the fabrication steps to realize arrays of tubular GMI sensor elements. a1) Patterning of the functional layer stack consisting of a sacrificial layer, expanding hydrogel layer and stiff polyimide layers. Each site will host a magnetic sensor device; a2) Realization of the electrical conductors and pick-up coils via deposition and photolithography. a3) Preparation of the magnetic GMI stack via deposition and photolithography. a4) Encapsulation of the devices using photopatternable polychloroprene layer. a5) Assembling the planar devices into compact tubular architectures by selectively etching the sacrificial layer. a6) Array of self-assembled GMI sensors with pick-up coils. Optical micrograph of an array of b) planar and e) self-assembled device. 3D map of the GMI response vs frequency and magnetic field measured of the c) planar and h) self-assembled device. Magnetic field dependences of the GMI response measured at 7 MHz and 75 MHz of d) planar and i) self-assembled structure. f) SEM image of the tube edge. g) FIB cut through the tube revealing 2 windings firmly attached to each other without forming voids.

evaporation (Figure 1a2). Then, another lift-off photoresist mask is brought onto the sample and the GMI stack consisting of $Ni_{81}Fe_{19}$(100 nm)/Cu(50 nm)/$Ni_{81}Fe_{19}$(100 nm) is grown using magnetron sputtering (Figure 1a3). To improve adhesion and protect the magnetic stack during lithographic processing, it is sandwiched by 2-nm-thick Ta layers. After the sensor layout is finalized, the sensor locations are covered by the photolithographically defined layer of polychloroprene rubber (thickness: 40 nm) leaving contact pads free of insulation for the electrical access for magnetoelectrical characterization (Figure 1a4).

By varying the 2D layout, different geometries of the electrodes and magnetic layers can be realized as shown in the optical micrograph in Figure 1b. The GMI response of the sensors is characterized in a probe station equipped with an electromagnet allowing us to apply magnetic fields of up to ±40 Oe in the substrate plane along the direction of the electrical current. By sweeping the external magnetic field at various frequencies of the driving current in the application relevant frequency range from 5 to 110 MHz, we plot the 3D map of the GMI ratio (Figure 1c). For high-performance sensorics, we are mainly interested in the sensitivity of the internal slopes of the GMI response. Hence, the GMI ratio is calculated as $\Delta Z/Z_0 = (|Z(H)|-|Z_0|)/|Z_0|$, where ΔZ is the difference between the absolute values of the impedance, Z, in an applied field, H, and the absolute impedance, Z_0, at zero applied field. For the planar sensors, we observe a standard two-peak GMI curve with a maximum value of about 1% (Z_0 = 0.5 Ohm), which is reached when the device is exposed to a magnetic field of 5 Oe

and driven by an AC current with 75 MHz excitation frequency (amplitude of the AC current is 1 mA) (see Figure 1d). The sensors are magnetically saturated in the field of about 20 Oe. The GMI performance of the reference planar devices is in-line with the previous literature reports.[39,51–53]

After precharacterization, the arrays of the planar sensor devices are protected by a 20 nm thick patterned layer of polychloroprene, and self-assembled into 3D magnetic architectures by selectively etching the sacrificial layer in a water-containing solution of 0.5 M sodium diethylenetriaminepentaacetic acid (DETPA). In the humid environment, the hydrogel-based polymer swells generating mechanical stress in the plane parallel to the reinforcing polyimide layer. This leads to an upward bending of the functional layer stack and initiates a rolling up process (Figure 1a5). After the etching process, the sample is washed in DI water solution with isopropanol in proportion 5:1 and dried at ambient conditions to form arrays of GMI sensors (Figure 1a6), homogeneously covering the entire substrate with an area of 22 × 22 mm^2 (Figure 1e). Experiments on larger substrates were not performed as those cannot be processed homogeneously using the available deposition chamber. However, the proposed fabrication approach imposes no limitations on the processing area to realize arrays of devices. Monitoring the quality of the self-assembly process over 400 rolled-up GMI devices allows us to quantify the fabrication yield—percentage of the properly rolled devices—to be better than 90%. The chosen thicknesses of the hydrogel and polyimide layers allow us to realize tubular structures with a diameter in the range of 50 µm and 2 windings (Figure 1f,g).

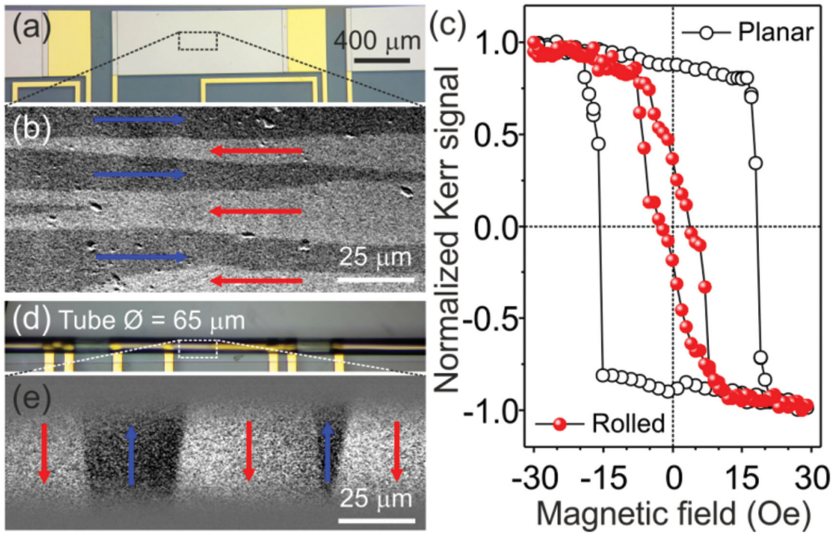

Figure 2. Magnetic properties of the GMI sensorics: a) Planar and d) self-assembled GMI device and the corresponding magnetic domain patterns of the GMI stack. Magneto-optical Kerr effect (MOKE) microscopy carried out on b) planar and e) self-assembled GMI elements. In the planar configuration a,b), the magnetic layer stack develops domains that are magnetized along the long side of the patterned rectangle. After the self-assembly d,e), an azimuthal domain pattern is observed. The orientation of the magnetic moment in the domains is indicated by arrows. c) Magnetic hysteresis loops measured using longitudinal MOKE magnetometry of the planar (open symbols) and self-assembled (filled symbols) devices. The external magnetic field is applied along the tube axis.

The GMI response of the rolled-up device is shown in Figure 1h,i. Direct comparison with its planar counterpart reveals that the rolled-up GMI sensor possesses a remarkable more than 80 times larger GMI ratio. The tubular sensor reveals a maximum GMI of about 90% at a 10 Oe applied field and 75 MHz excitation. Applying the magnetic field along the tube axis does not bring the GMI response to saturation in the available magnetic field range of 40 Oe at frequencies above 20 MHz. This finding indicates the stabilization of the circumferential anisotropy, which results from the geometrical transformation from the planar layout to the tubular-shaped GMI sensor.

To confirm this assumption and understand the origin of the GMI response in the samples, we performed detailed investigation of the magnetization reversal processes and magnetic domain patterns of the samples in planar and rolled-up arrangements (**Figure 2**). For this purpose, longitudinal magneto-optical Kerr effect (MOKE) magnetometry and microscopy was carried out.[54] Due to the rectangular shape of the planar layout (footprint: 2 × 1 mm^2), the magnetic domains are magnetized preferentially along the long axis of the sample (Figure 2a,b), which is the easy axis of magnetization as derived from the analysis of the magnetic hysteresis loops (Figure 2c). The coercive field of the planar samples is less than 20 Oe (Figure 2c), which is typical for sputter-deposited $Ni_{81}Fe_{19}$ thin films due to their non-zero magnetostriction.[55]

The magnetic domains are visualized using the longitudinal magneto-optical Kerr microscopy. The spot size of the focused beam in the MOKE magnetometry set-up was approximately 100 × 100 µm^2, which allows us to study the magnetic response of individual rolled-up architectures.[56,57] Similar to imaging using soft X-ray microscopy[58] and tomography,[59] magneto-optical Kerr microscopy provides important insight into the magnetic microstructure of the 3D samples possessing domains with a size in the micrometer range. Imaging was performed by applying an external magnetic field parallel to the tube axis. Taking into account the limited probing depth of the Kerr effect of approximately 20 nm[60] and the curvature of the object, only information about the magnetic state of the outer layer along a narrow stripe on top of the tube can be obtained. The magnetization orientation within the dark and bright domains is indicated by arrows. The geometrical transformation of the planar GMI stack into the 3D tubular architecture results in the drastic modification of the magnetic domain pattern (Figure 2d,e) leading to the stabilization of azimuthal domains[57] with a characteristic size of about 20 µm separated by domain walls slightly tilted relative to the tube axis.[56] This circular domain pattern, which provides flux closure around the tubular geometry, is stress-driven due to non-zero positive magnetostriction of the thin films of $Ni_{81}Fe_{19}$. This observation is in line with the transformation of the shape of the magnetic hysteresis into a typical hard axis loop when measured in a field applied along the tube axis (Figure 2c). The appearance of the azimuthal domain pattern with circumferential magnetization,

ADVANCED MATERIALS
www.advmat.de

Materials Views
www.MaterialsViews.com

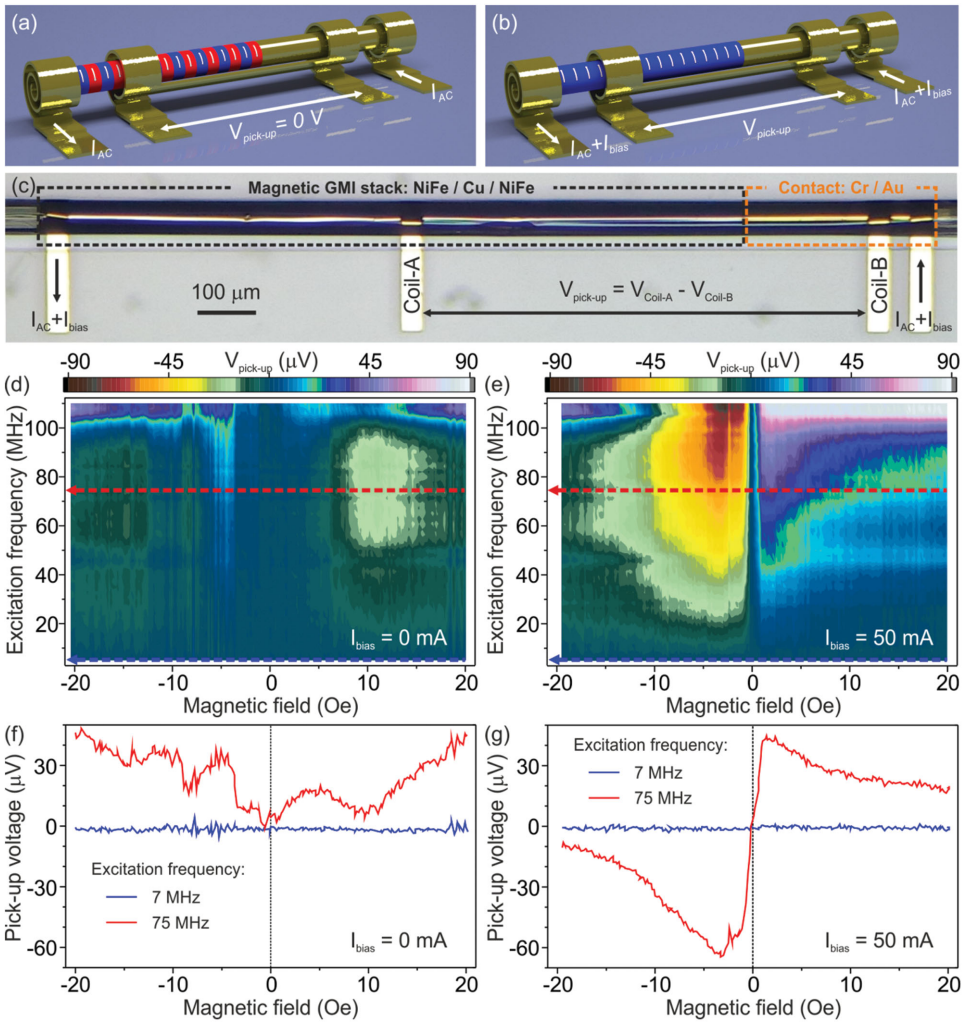

Figure 3. Integrated GMI sensor with a pick-up coil: a,b) Schematics showing the rolled-up GMI sensor with a set of two asymmetrically wound but otherwise identical pick-up coils. Outer contacts are used to measure the GMI effect. Inner contacts correspond to the pick-up coil. Coil-A is wound around the magnetic stack; Coil-B acts as a reference coil wound around the non-magnetic conducting part of the structure. Coil-A and Coil-B are connected in series. Panel a) schematizes the multidomain magnetic state of the device with no longitudinal DC bias current applied. b) Applying a sufficiently large DC bias current results in the single domain azimuthally magnetized tubular architecture. c) Optical micrograph of the real device accommodating two asymmetrically placed peak-up coils around a GMI element. 3D map of the pick-up voltage vs frequency and magnetic field measured d) without DC current bias and e) with DC bias current of 50 mA. Magnetic field dependences of the pick-up voltage taken at the excitation frequencies of 7 and 75 MHz when the device is measured f) without DC current bias and g) with DC bias current of 50 mA. The excitation AC current is 1 mA.

which is oriented preferentially perpendicular to the direction of the electrical current, explains the observed enhancement of the GMI effect in the rolled-up samples compared to their planar counterparts. The possibility of stabilizing the peculiar azimuthal domain pattern, which is of advantage for the enhancement of the GMI effect, via the geometrical transformation upon self-assembly into a tubular architecture can be used to realize GMI devices in a CMOS compatible process. Indeed, the thermal annealing step, which is needed to induce circumferential magnetization in magnetic microwires and thin films,[31,32] can be safely omitted.

The key feature of the developed technology platform is the possibility to integrate multiple functional elements in a single architecture. Aiming for on-chip-integrated GMI sensorics, this feature is of great advantage as we can produce a pick-up coil simultaneously during the self-assembly of the GMI layer stack (**Figure 3**a–c). The pick-up coil is produced in the same lithographic process together with the formation of the electrical contacts (Figure 1a2). This simplifies the design of the sensor device as the number of processing steps can be substantially reduced. The preparation of the pick-up coil requires only one lithography step in comparison to the multistep lithography typically used for its fabrication.[39] The planar layout for the pick-up coil is designed in a way to use a single conductor path forming a coil with about two windings around the GMI element. For the self-assembled GMI sensorics, this implies that two coils are formed as the contact electrodes are always on one side of the assembled rolled-up architecture: the first one, indicated as pick-up Coil-A in Figure 3c, is wound around the magnetic part and the second Coil-B is wound around the

nonmagnetic part of the GMI device. In this scheme, the oppositely wounded, identical coils are detuned from their compensation point by the presence of the GMI stack within one of the coils. Therefore, we can detect the longitudinal gyrotropic component of the magnetization precession. The measurement is performed as follows: the excitation AC current of 1 mA at different frequencies is supplied to the GMI element and the pick-up voltage from the pick-up coil is measured as a function of magnetic field in the range of −40 to +40 Oe with the excitation frequency as sweep parameter changing between 5 and 110 MHz (Figure 3d,e). As pick-up voltage we define the voltage difference measured in Coil-A and Coil-B. Independent of the realized rolled-up geometry, the behavior of the observed GMI effect is similar to the one reported for amorphous microwires measured using pick-up coils.[39] Indeed, we observe a strong dependence of the effect upon a DC biasing current sent through the sensor (compare Figure 3d,e). We exemplarily show two qualitatively distinct characteristics measured at 0 and 50 mA bias current. For no bias applied, hardly any pick-up signal from the GMI element is observed. This statement is supported by the analysis of the magnetic field dependences of the GMI taken at the excitation frequencies of 7 and 75 MHz (Figure 3f). This finding is in-line with the results reported by Fry et al.,[39] where the absence of the pick-up measured GMI response was attributed to the compensation of the gyrothropic components stemming from oppositely magnetized domains. This is typical for the devices, where the magnetic domain size is smaller than the width of the pick-up coil (Figure 3a).

By applying a DC bias current, the domain structure of the magnetic tube is affected by the Oersted field. Depending on the current direction, a left- or right-handed circular magnetic field can be generated, which imposes the preference to one of the azimuthally magnetized domains. In sufficiently large DC bias currents of 50 mA, the size of domains is larger than the width of the pick-up coil (40 µm), leading to a measurable GMI signal at the pick-up coil as it was shown for magnetic wires using Kerr microscopy by Stupakiewicz et al.[54] As follows from magneto-optical Kerr microscopy imaging, the DC bias current of 50 mA produces a strong enough Oersted field, which completely magnetizes the tubular structure in circumferential direction (schematically shown in Figure 3b) forming a single domain state. This leads to rather strong GMI response as shown in Figure 3e,g. The sensitivity of the sensor at the excitation frequency of 75 MHz is 45 µV Oe^{-1} (zero-field pick-up voltage is 6 mV). Recalculating to the parameters of our device with the current of 1 mA and number of turns of the coil equal 2, the state-of-the-art devices that are using preamplification circuits with a gain of >100 reveal responsivities in the range from 15 µV Oe^{-1} up to 1 mV Oe^{-1}.[17,23,26,61–63]

In conclusion, we put forth a novel method relying on strain engineering to realize on-chip-integrated GMI sensors. The key advantages offered by the self-assembly approach to realize high-performance GMI devices are: i) a geometrical transformation from the initially planar layout into a tubular 3D architecture allows to achieve favorable circular magnetic domain patterns without the need of rapid quenching of the magnetic layer stack in a magnetic field; ii) we can integrate multiple functional elements in a single architecture including GMI sensors and pick-up coils, which are produced simultaneously in a single fabrication run. As the high temperature processing of the layer stack can be safely omitted, this renders our technology platform CMOS compatible. Indeed, the used polymeric materials and the individual fabrication steps, e.g., thin film deposition and optical lithography at 405 nm exposure light, comply with the requirements imposed on conventional CMOS electronics.

This work creates a solid foundation for further development of CMOS compatible GMI sensorics for magnetoencephalography applications. On-chip-integrated GMI sensors are compact and do not require helium cooling. Hence, the sensing element can be positioned at a distance of less than 10 mm from the current element (electric current flow of a local population of active neurons; typically 2 to 100 nAm[6,7]) generating the magnetic field. The much smaller distance to the source of the magnetic field is the key advantage over SQUID devices, which are typically located at a distance of 50 mm leading to rather low magnetic fields of 80 fT–4 pT to be detected.[6] Magnetic fields of the current element decrease with the square of the distance. Therefore, the field to be measured at a distance of 10 mm is 2 pT–100 pT, which is easily detectable using GMI sensors.[27] In this respect, the used in this work NiFe/Cu/NiFe material combination may be seen as a model system to achieve the GMI effect of about 100%. Still, a drastic improvement in sensitivity is envisioned by utilizing magnetically soft high-moment materials such as CoFeSiB.[64,65] Furthermore, arrays of sensors should be produced in a special manner to realize magnetic field gradiometers based on GMI sensorics as needed for magnetoencephalography applications.[6]

Experimental Section

Treatment of the Substrate: Cover glasses with dimensions of 22×22 mm^2 and a thickness of 150 µm (Menzel cover glasses) were used as a handling substrate. First, the substrates were sonicated for 5 min by immersing them in acetone and isopropanol and subsequently rinsed in the deionized (DI) water. Then, the substrates were sonicated for 30 min in a 2% water solution of Alconox cleaner (Alconox Inc.) and rinsed thoroughly using DI water under ultrasonic conditions. After cleaning, the substrates were kept in DI water to prevent them from contamination and keep the surface hydrolyzed.

Adhesion Layer: For better adhesion of the polymeric layers, the substrates were modified for 20 min with self-assembled monolayers of 3-(trimethoxysilyl) propyl methacrylate (Polysciences Europe GmbH) in a 1.5% (v/v) mixture of silane in toluene (Sigma–Aldrich Co. LLC., Germany). Afterwards, the substrates were washed in toluene, dried using nitrogen gas, and baked on a hotplate at 120 °C for 5 min under nitrogen atmosphere.

Sacrificial Layer: The polymeric sacrificial layer was fabricated using acrylic acid (AA) (Alfa Aesar) and hydrated $LaCl_3$ (Alfa Aesar). A mixture of 10 g AA with 4.86 g of $LaCl_3$ in water provided an LaAA precipitate. This precipitate was collected through a filter paper in an exicator, where it was dried at 40 °C for 10 h. Further, the obtained material was dissolved in AA at a concentration of 25% (w/w) and photosensitized using 2% (w/w) of 2-benzyl-2-(dimethylamino)-4-morpholinobutyrophenone and 3% (w/w) methyl diethanolamine (Sigma–Aldrich Co. LLC., Germany). The sacrificial layer solution was spin-coated at 3000 rpm for 35 s to produce a 160 nm thick layer. Drying was carried out at 35 °C for 2 min with the subsequent exposure to a 405 nm mercury h-line (20 mW cm^{-2}) for 15 s through a glass/Cr mask using a SUSS MA4 (Karl Suss KG–Gmbh & Co, Munchen-Garching, Germany) mask aligner. Development was done in DI water for 5 s with a subsequent rinsing in (1-methoxy-2-propyl) acetate (Sigma-Aldrich Co.

LLC., Germany). Finally, the samples were annealed at 200 °C for 5 min under nitrogen atmosphere to remove all solvent residuals.

Strained Bilayers: The differential strain in the polymeric bilayer was introduced by swelling one of the polymers in an aqueous media. The other layer was kept in a non-swollen state operating as a single-layer reinforcement.

The solution for the swelling layer was prepared by reaction of *N*-(2-hydroxyethyl)acrylamide (HEAA) and poly(ethylene-*alt*-maleic anhydride) (PEMA) in *N,N*-dimethylacetamide (DMAc), which was photosensitized by 2% (w/w) of 2-benzyl-2-(dimethylamino)-4-morpholinobutyrophenone (Sigma-Aldrich Co. LLC., Germany). Here, 6 g of PEMA was dissolved in 50 mL DMAc and 5.75 g of HEAA was added. The reaction was carried out for 10 h at room temperature. The solution was spin coated at 4000–8000 rpm for 35 s, resulting in layer thicknesses of 300–150 nm, respectively. After drying the polymeric layer at 50 °C for 5 min, the sample was exposed to a 405 nm mercury h-line (20 mW cm^{-2}) for 1.5 min through a glass/Cr mask using a SUSS MA4 mask aligner. The development was done in a mixture of 1 part DMAc and 2 parts of propylene carbonate (Sigma–Aldrich Co. LLC., Germany) for 30 s with a subsequent rinsing in isopropanol. Finally, the sample was annealed at 200 °C for 5 min under a nitrogen atmosphere to remove the residual solvent.

Polyimide was used as the nonswelling layer. The photosensitive polyimide was synthesized by the reaction of 3,3′,4,4′-benzophenonetetracarboxylic dianhydride (BPDA) and 3,3′-diaminodiphenylsulfone (DADPS) in *N,N*-dimethylacetamide (DMAc), modified with dimethylaminoethyl methacrylate (DMAEMA) and photosensitized by 2% (w/w) of 2-benzyl-2-(dimethylamino)-4-morpholinobutyrophenone (Sigma–Aldrich Co. LLC., Germany). The polymer synthesis was carried out by dissolution of 9.93 g DADPS in 20 mL DMAc with the subsequent addition of 12.8 g of BPDA. After mixing for 12 h at 70 °C, the solution of polyamic acid (PAA) in DMAc was achieved. The solution of PAA was neutralized by reaction with 12.5 g of DMAEMA. The polymer was spin coated at 2000–8000 rpm for 35 s, resulting in the layer thickness of 1700–500 nm, respectively. After drying the polymeric layer at 50 °C for 10 min, the sample was exposed to a 405 nm mercury h-line (20 mW cm^{-2}) for 1.5 min through a glass/Cr mask using a SUSS MA4 mask aligner.

Development was done in a mixture of 1 part (v/v) 1-ethyl-2-pyrrolidone, 0.58 parts (v/v) of methyl alcohol and 0.50 parts (v/v) of diethylene glycol monoethyl ether for 1 min with the subsequent rinsing in propylene glycol monomethyl ether acetate (Sigma-Aldrich Co. LLC., Germany). The imidization process of the achieved structures was performed on a hotplate at 200 °C for 5 min under a nitrogen atmosphere simultaneously removing the residual solvent.

Fabrication of Devices in the Planar Arrangement: The magnetic layer stack was composed of $Ni_{81}Fe_{19}$(100 nm)/Cu(50 nm)/$Ni_{81}Fe_{19}$(100 nm), which was prepared via magnetron sputter deposition in a high-vacuum chamber (base pressure: 4×10^{-7} mbar; Ar sputter pressure: 6×10^{-4} mbar; deposition rate: 0.2 Å s^{-1}). To improve adhesion and to protect the magnetic stack while lithographic processing, it was sandwiched with 2 nm thick Ta layers. Sputtering from the $Ni_{80}Fe_{20}$ target material resulted in a composition shift in the resultant alloy film to $Ni_{81}Fe_{19}$ with a non-zero magnetostriction of this alloy.[55,66] In particular, for $Ni_{81}Fe_{19}$ thin films, increased values of the saturation magnetostriction, λ_s, were attributed to interfacial effects.[67]

The electrical contacts as well as pick-up coils were realized using Cr(5 nm)/Au(50 nm) bilayers prepared via the electron beam evaporation (base pressure: 1×10^{-6} mbar; deposition rate: 2 Å s^{-1}). The width of the contacts was 40 µm. Each functional layer including contacts, sensors, and pick-up coils was patterned using standard UV lithography by lifting-off the underlying photoresist layer.

In a single fabrication process, the array of devices over the entire 22×22 mm^2 substrate was defined. Each functional element containing the GMI sensor was accommodated at the area of 1×1 mm^2 resulting in about 400 devices per sample.

Protecting Layer: Before the self-assembly process, the sensors and electrical contacts were protected by photopatternable polychloroprene leaving only the contact pads free for the magnetoelectrical characterization. The photosensitive polychloroprene was prepared from a mixture of polychloroprene (0.75 g) in 25 mL of 3 parts (v/v) of cyclopentanone/1 part (v/v) of 1-methoxy-2-propanole. In the mixture, 50 mg of 2-benzyl-2-(dimethylamino)-4-morpholinobutyrophenone and 150 mg of pentaerythritol triacrylate were added. The solution was stirred for 2 h and then spin-coated at 6000 rpm for 35 s, resulting in a layer thickness of 100 nm. The sample was exposed to a 405 nm mercury h-line (20 mW cm^{-2}) for 1.5 min through a glass/Cr mask using a SUSS MA4 mask aligner. The development was done by washing the sample in 4-methyl-2- pentanone for 5 s. All chemicals were obtained from Sigma-Aldrich Co. LLC, Germany.

Self-Assembly Process into Tubular Architectures: The planar 2D layouts were self-assembled into 3D Swiss rolls by selectively etching the sacrificial layer in a solution of 0.5 M sodium diethylenetriaminepentaacetic acid (DTPA) (Alfa Aesar, UK). After the etching process, the structures were washed in DI water. Then the tubes were placed in a solution of DI water and isopropanol in proportion 1:5 and dried at ambient conditions. The tubes homogeneously covered the entire area of the substrate with an area of 22×22 mm^2. Monitoring the quality of the self-assembly process over 400 rolled-up GMI devices allowed us to quantify the fabrication yield to be better than 90%.

For the case of the sensors complemented with the pick-up coil, 10 sites for tubular structures were formed on the substrate with an area of 22×22 mm^2. Each site hosted the layout for 10× identical GMI elements with pick-up coils, which were rolled-up into a single tubular architecture. The self-assembly process was optimized to have all 100 devices operational after the rolling-up process.

Electrical Characterization: The magnetoelectrical characterization of planar reference samples as well as samples rolled-up into compact tubular architectures was carried out using a probe station equipped with an electromagnet. The samples were electrically contacted using tungsten probe tips fixed in micromanipulators. The impedance was measured using an Agilent 4294A impedance analyzer equipped with coaxial probes. Characterization was done in the frequency range of 5 MHz–110 MHz. Magnetic fields were applied in the substrate plane parallel to the direction of the electrical current. The magnetic field was controlled with a precision of better than 0.1 Oe using the Hall probe.

Imaging of Magnetic Domains: Magnetic imaging was performed using longitudinal and transversal magneto-optical Kerr microscopy on planar samples as well as on tubular structures. The magnetic state of the samples was altered by exposing the samples to an in-plane magnetic field of –1000 Oe to 1000 Oe using an electromagnet. Please note that due to the curvature, only a narrow stripe on top of the tube could be imaged in-focus during imaging.

Acknowledgement

The authors thank I. Fiering and C. Krien (IFW Dresden) for the deposition of the metal layer stacks. The support of the clean room team headed by Dr. S. Harazim (IFW Dresden) was greatly appreciated. This work was financed in part via the European Research Council within the European Union's Seventh Framework Programme (FP7/2007–2013)/ ERC grant agreement no. 306277, German Science Foundation (DFG) grant MA 5144/2-1 and DFG Research Group FOR1713.

Received: June 28, 2015
Revised: August 17, 2015
Published online: September 23, 2015

[1] J. Viventi, D.-H. Kim, J. D. Moss, Y.-S. Kim, J. A. Blanco, N. Annetta, A. Hicks, J. Xiao, Y. Huang, D. J. Callans, J. A. Rogers, B. Litt, *Sci. Transl. Med.* **2010**, *2*, 24ra22.

[2] Z. M. Williams, *Nat. Neurosci.* **2015**, *18*, 618.
[3] A. B. Schwartz, *Annu. Rev. Neurosci.* **2004**, *27*, 487.
[4] C. Grau, R. Ginhoux, A. Riera, T. L. Nguyen, H. Chauvat, M. Berg, J. L. Amengual, A. Pascual-Leone, G. Ruffini, *PLoS One* **2014**, *9*, e105225.
[5] F. A. Mussa-Ivaldi, L. E. Miller, *Trends Neurosci.* **2003**, *26*, 329.
[6] R. Hari, R. Salmelin, *Neuroimage* **2012**, *61*, 386.
[7] M. Hämäläinen, R. Hari, R. J. Ilmoniemi, J. Knuutila, O. V. Lounasmaa, *Rev. Mod. Phys.* **1993**, *65*, 413.
[8] M. A. Lebedev, M. A. L. Nicolelis, *Trends Neurosci.* **2006**, *29*, 536.
[9] M. E. Funke, K. Moore, W. W. Orrison, J. D. Lewine, *Epilepsia* **2011**, *52*, 10.
[10] M. Pannetier, C. Fermon, G. Le Goff, J. Simola, E. Kerr, *Science* **2004**, *304*, 1648.
[11] X. Navarro, T. B. Krueger, N. Lago, S. Micera, T. Stieglitz, P. Dario, *J. Peripher. Nerv. Syst.* **2005**, *10*, 229.
[12] M. A. L. Nicolelis, *Nat. Rev. Neurosci.* **2003**, *4*, 417.
[13] T. H. Sander, J. Preusser, R. Mhaskar, J. Kitching, L. Trahms, S. Knappe, *Biomed. Opt. Express* **2012**, *3*, 981.
[14] O. Alem, A. M. Benison, D. S. Barth, J. Kitching, S. Knappe, *J. Neurosci.* **2014**, *34*, 14324.
[15] L. V Panina, K. Mohri, K. Bushida, M. Noda, *J. Appl. Phys.* **1994**, *76*, 6198.
[16] Y. Nishibe, H. Yamadera, N. Ohta, K. Tsukada, Y. Nonomura, *Sens. Actuators, A Phys.* **2000**, *82*, 155.
[17] B. Dufay, S. Saez, C. Dolabdjian, A. Yelon, D. Menard, *IEEE Trans. Magn.* **2013**, *49*, 85.
[18] M. Vázquez, H. Chiriac, A. Zhukov, L. Panina, T. Uchiyama, *Phys. Status Solidi Appl. Mater. Sci.* **2011**, *208*, 493.
[19] M. Malátek, L. Kraus, *Sens. Actuators, A Phys.* **2010**, *164*, 41.
[20] F. L. A. Machado, S. M. Rezende, *J. Appl. Phys.* **1996**, *79*, 6558.
[21] L. A. Tuan, N. T. Huy, P. T. Huy, *J. Phys.: Conf. Ser.* **2009**, *187*, 012044.
[22] A. Chaturvedi, N. Laurita, A. Leary, M. H. Phan, M. E. McHenry, H. Srikanth, *J. Appl. Phys.* **2011**, *109*, 5.
[23] K. Mohri, T. Uchiyama, L. P. Shen, C. M. Cai, L. V. Panina, Y. Honkura, M. Yamamoto, *IEEE Trans. Magn.* **2002**, *38*, 3063.
[24] T. Uchiyama, K. Mohri, S. Nakayama, *IEEE Trans. Magn.* **2011**, *47*, 3070.
[25] M.-H. H. Phan, H.-X. X. Peng, *Prog. Mater. Sci.* **2008**, *53*, 323.
[26] T. Uchiyama, S. Nakayama, *Physiol. Rep.* **2013**, *1*, e00030.
[27] S. Nakayama, K. Sawamura, K. Mohri, T. Uchiyama, *PLoS One* **2011**, *6*, e25834.
[28] T. Uchiyama, N. Hamada, C. Cai, *IEEE Trans. Magn.* **2014**, *50*, 4005404.
[29] T. Morikawa, Y. Nishibe, H. Yamadera, Y. Nonomura, M. Takeuchi, J. Sakata, Y. Taga, *IEEE Trans. Magn.* **1996**, *32*, 4965.
[30] T. Morikawa, Y. Nishibe, H. Yamadera, Y. Nonomura, M. Takeuchi, Y. Taga, *IEEE Trans. Magn.* **1997**, *33*, 4367.
[31] P. Delooze, L. V. Panina, D. J. Mapps, K. Ueno, H. Sano, *IEEE Trans. Magn.* **2003**, *39*, 3307.
[32] P. Delooze, L. V. Panina, D. J. Mapps, K. Ueno, H. Sano, *J. Magn. Magn. Mater.* **2004**, *272–276*, 2266.
[33] O. G. Schmidt, K. Eberl, *Nature* **2001**, *410*, 168.
[34] V. Y. Prinz, V. A. Seleznev, A. K. Gutakovsky, A. V. Chehovskiy, V. V. Preobrazenskii, M. A. Putyato, T. A. Gavrilova, *Phys. E* **2000**, *6*, 828.
[35] L. Ionov, *Mater. Today* **2014**, *17*, 494.
[36] Y. Mei, G. Huang, A. A. Solovev, E. B. Ureña, I. Mönch, F. Ding, T. Reindl, R. K. Y. Fu, P. K. Chu, O. G. Schmidt, *Adv. Mater.* **2008**, *20*, 4085.
[37] D. D. Karnaushenko, D. Karnaushenko, D. Makarov, O. G. Schmidt, *NPG Asia Mater.* **2015**, *7*, e188.
[38] D. de Cos, N. Fry, I. Orue, L. V. Panina, A. Garcia-Arribas, J. M. Barandiaran, *Sens. Actuators, A Phys.* **2006**, *129*, 256.
[39] N. Fry, D. P. Makhnovskiy, L. V. Panina, S. I. Sandacci, D. J. Mapps, M. Akhter, *IEEE Trans. Magn.* **2004**, *40*, 3358.
[40] J. C. Lin, *IEEE Antennas Propag. Mag.* **2006**, *48*, 157.
[41] J. Reeder, M. Kaltenbrunner, T. Ware, D. Arreaga-Salas, A. Avendano-Bolivar, T. Yokota, Y. Inoue, M. Sekino, W. Voit, T. Sekitani, T. Someya, *Adv. Mater.* **2014**, *26*, 4967.
[42] A. R. Studart, R. M. Erb, *Soft Matter* **2014**, *10*, 1284.
[43] T. G. Leong, P. A. Lester, T. L. Koh, E. K. Call, D. H. Gracias, *Langmuir* **2007**, *23*, 8747.
[44] G. Stoychev, N. Puretskiy, L. Ionov, *Soft Matter* **2011**, *7*, 3277.
[45] R. Fernandes, D. H. Gracias, *Adv. Drug Delivery Rev.* **2012**, *64*, 1579.
[46] V. Stroganov, S. Zakharchenko, E. Sperling, A. K. Meyer, O. G. Schmidt, L. Ionov, *Adv. Funct. Mater.* **2014**, *24*, 4357.
[47] V. Luchnikov, O. Sydorenko, M. Stamm, *Adv. Mater.* **2005**, *17*, 1177.
[48] S. Zakharchenko, E. Sperling, L. Ionov, *Biomacromolecules* **2011**, *12*, 2211.
[49] L. Ionov, *Macromol. Chem. Phys.* **2013**, *214*, 1178.
[50] V. Luchnikov, L. Balan, *Nanomater. Nanotechnol.* **2014**, *4*, 20.
[51] D. P. Makhnovskiy, N. Fry, L. V. Panina, D. J. Mapps, *J. Appl. Phys.* **2004**, *96*, 2150.
[52] B. Li, M. N. Kavaldzhiev, J. Kosel, *J. Magn. Magn. Mater.* **2015**, *378*, 499.
[53] D. P. Makhnovskiy, L. V. Panina, N. Fry, D. J. Mapps, *J. Magn. Magn. Mater.* **2004**, *272–276*, 1866.
[54] A. Stupakiewicz, A. Chizhik, M. Tekielak, A. Zhukov, J. Gonzalez, A. Maziewski, *Rev. Sci. Instrum.* **2014**, *85*, 103702.
[55] C.-Y. Hung, M. Mao, S. Funada, T. Schneider, L. Miloslavsky, M. Miller, C. Qian, H. C. Tong, *J. Appl. Phys.* **2000**, *87*, 6618.
[56] R. Streubel, D. Makarov, J. Lee, C. Müller, M. Melzer, R. Schäfer, C. C. B. Bufon, S.-K. Kim, O. G. Schmidt, *Spin* **2013**, *3*, 1340001.
[57] R. Streubel, J. Lee, D. Makarov, M.-Y. Y. Im, D. Karnaushenko, L. Han, R. Schäfer, P. Fischer, S.-K. K. Kim, O. G. Schmidt, *Adv. Mater.* **2014**, *26*, 316.
[58] R. Streubel, L. Han, F. Kronast, A. A. Ünal, O. G. Schmidt, D. Makarov, *Nano Lett.* **2014**, *14*, 3981.
[59] R. Streubel, F. Kronast, P. Fischer, D. Parkinson, O. G. Schmidt, D. Makarov, *Nat. Commun.* **2015**, *6*, 7612.
[60] A. Hubert, R. Schäfer, *Magnetic Domains: The Analysis of Magnetic Microstructures,* Springer-Verlag, Berlin Heidelberg, Germany **2009**.
[61] T. Uchiyama, K. Mohri, Y. Honkura, L. V. Panina, *IEEE Trans. Magn.* **2012**, *48*, 3833.
[62] B. Dufay, S. Saez, C. P. Dolabdjian, A. Yelon, D. Menard, *IEEE Sens. J.* **2011**, *11*, 1317.
[63] B. Dufay, S. Saez, C. P. Dolabdjian, A. Yelon, D. Menard, *IEEE Sens. J.* **2013**, *13*, 379.
[64] D. P. Makhnovskiy, L. V. Panina, D. J. Mapps, *Appl. Phys. Lett.* **2000**, *77*, 121.
[65] P. Ripka, *Magnetic Sensors and Magnetometers,*Artech House Inc., Boston, MA, USA **2001**.
[66] N. Pérez, M. Melzer, D. Makarov, O. Ueberschär, R. Ecke, S. E. Schulz, O. G. Schmidt, *Appl. Phys. Lett.* **2015**, *106*, 153501.
[67] M. P. Hollingworth, M. R. J. Gibbs, S. J. Murdoch, *J. Appl. Phys.* **2003**, *94*, 7235.